Materials Transactions, Vol. 42, No. 4 (2001) pp. 642 to 649
Special Issue on Bulk Metallic Glasses III

Deformation Mechanisms of the $Zr_{40}Ti_{14}Ni_{10}Cu_{12}Be_{24}$ Bulk Metallic Glass

Wendelin J. Wright, Ranjana Saha and William D. Nix

Department of Materials Science & Engineering, Stanford University, Stanford, CA 94305-2205, USA

We have studied the mechanical behavior of $Zr_{40}Ti_{14}Ni_{10}Cu_{12}Be_{24}$ through uniaxial compression and nanoindentation experiments. Quantitative measurements of the serrated plastic flow observed during uniaxial compression are reported. These data are used to predict temperature increases in single shear bands due to local adiabatic heating caused by the work done on the sample as shear propagates progressively across the sample. Since the predicted temperature increases are insufficient to reach the glass transition temperature, it is unlikely that localized heating is the primary cause of flow localization. Instead, localization of shear is more likely caused by changes in viscosity associated with increased free volume in the shear bands. The orientation of the shear bands in compression tests and an indentation size effect for the onset of plastic flow in nanoindentation both point to increased free volume as the cause of localization.

(Received January 9, 2001; Accepted January 29, 2001)

Keywords: *adiabatic heating, amorphous metal, free volume, metallic glass, Mohr-Coulomb, nanoindentation, serrated flow*

1. Introduction

Prior to the development of bulk metallic glasses, specimens for mechanical testing of amorphous metals were available only in ribbon form. Investigations of mechanical behavior were thus confined to tension and bend testing. Because metallic glasses cannot sustain plastic strain in tension, limited information about their flow properties was available. The development of bulk metallic glasses[1,2] enabled a wider range of mechanical tests including compression, torsion, fracture toughness, and fatigue testing.[3–7] Consequently, the bulk macroscopic mechanical properties of metallic glasses have now been thoroughly investigated. Nonetheless, the precise nature of the deformation mechanisms in these amorphous materials remains unclear.

Flow in metallic glasses is extremely inhomogeneous at high stresses and low temperatures. Deformation is localized in thin shear bands near planes of maximum shear and appears to be related to a local change in viscosity within these bands. There are two hypotheses as to why this may be the case. The first suggests that, during deformation, the viscosity within the shear bands decreases due to the formation of free volume, which in turn decreases the density of the glass. This hypothesis originated in the work of Spaepen, who derived an expression for steady-state inhomogeneous flow in metallic glasses based on a competition between stress-driven creation and diffusional annihilation of free volume.[8] Argon then demonstrated that flow localizes in a band of material in which the strain rate has been perturbed due to the creation of free volume.[9] Subsequently, Steif, Spaepen, and Hutchinson extended Spaepen's model by deriving an expression for the stress at which catastrophic softening due to free volume creation occurs during uniform shearing of a homogeneous body under constant applied strain rate.[10] This expression agrees well with their numerical solution for the stress at strain localization in a shear band, based on the mechanics of an infinite body containing a band of slightly weaker material.

The second hypothesis to explain reductions in shear band viscosity contends that local adiabatic heating beyond the glass transition temperature, or even the melting temperature, occurs, decreasing the viscosity by several orders of magnitude. This idea was proposed by Leamy, Chen, and Wang who attributed the vein pattern morphology of fracture surfaces to adiabatic heating of the deformed region.[11] Later, Liu *et al.* detected sparking from tension samples during the moment of fracture and observed liquid droplets at major cracks adjacent to the fracture surfaces of these samples.[12] By assuming that all of the elastic strain energy stored in a sample at the moment of tensile fracture was dissipated as heat on the fracture plane, they estimated temperature increases of 900 K. This hypothesis gained further support based on the results of dynamic compression testing by Bruck, Rosakis, and Johnson.[13] Temperature increases of nearly 775 K were observed using high-speed infrared detection; it should be noted, however, that the strain rates imposed in these tests were more than six orders of magnitude higher than those imposed during quasi-static uniaxial compression testing. The calculated or measured temperature increases cited here are applicable only to fracture events and do not apply to the inhomogeneous deformation that occurs prior to failure.

Although the cause of the viscosity reduction is disputed, it is clear that it localizes the deformation and leads to inhomogeneous flow in metallic glasses. In this paper, we present the results of uniaxial compression testing and nanoindentation that support the free volume theory of deformation. Quantitative measurements of serrated flow during compression testing are reported. These data are used to predict temperature increases in single shear bands due to local adiabatic heating caused by the work done on the sample during plastic deformation. Since the predicted temperature increases are insufficient to reach the glass transition temperature, it seems unlikely that localized heating is the primary cause of flow localization. A Mohr-Coulomb analysis of the orientation of shear bands formed in uniaxial compression indicates that normal stresses affect shear band propagation; a normal stress dependence is expected with the free volume theory. Finally, nanoindentation results demonstrate a dependence of the shear strength on indentation size that is also consistent with the free volume theory.

2. Serrated Flow and Shear Band Formation

The inhomogeneous nature of the deformation in metallic glasses is manifested in serrated plastic flow. During uniaxial compression testing, metallic glass samples load elastically to the yield stress, at which point serrated plastic flow begins. Serrated flow is characterized by repeating cycles of a sudden stress drop followed by elastic reloading.[14] While the origin of serrated flow in metallic glasses is uncertain, it is surely related to the formation of shear bands. The aim of this work was to better understand deformation in metallic glasses and its underlying mechanisms by studying serrated flow in detail.

2.1 Experimental procedures

Samples were prepared from the $Zr_{40}Ti_{14}Ni_{10}Cu_{12}Be_{24}$ metallic glass alloy that was provided by Howmet Research Corporation (Whitehall, MI) in plate form. Rectangular samples with 2:1 and 3:1 aspect ratios (4 mm long and 2 mm on each side and 6 mm long and 2 mm on each side) were electrode discharge machined from the cast material. Since these samples were to be tested in compression, the square faces were ground parallel. The rectangular faces were mechanically polished with a dispersion of 0.05 μm alumina particles.

An Instron model 1125 screw-driven mechanical test system was used to perform uniaxial compression tests at a constant displacement rate. A 5000 kg load cell measured the applied load, and two linear variable differential transformers (LVDTs) measured sample displacements. The LVDT conditioners were equipped with 400 Hz active low-pass filters. The LVDTs were connected directly to the platens. This arrangement allowed for direct measurement of sample displacements, eliminating the need to account for machine or load cell stiffness. The axially symmetric arrangement of the LVDTs compensated for any bending of the sample during deformation. The tests were performed with a nominal strain rate of $10^{-4}\,s^{-1}$. The data acquisition system permitted collection rates of up to 100 measurements per second.

2.2 Experimental results

Figure 1 shows the stress-strain curve for $Zr_{40}Ti_{14}Ni_{10}Cu_{12}Be_{24}$ tested in uniaxial compression. The yield stress and elastic modulus of $Zr_{40}Ti_{14}Ni_{10}Cu_{12}Be_{24}$ were 1.9 and 97 GPa, respectively. These values are similar to those reported by others for nearly identical alloys.[5]

Multiple serrations were observed in each of the compression tests. As these represent an important contribution to the plasticity of the material, the magnitude of the load drop, the displacements (total, elastic, and plastic), and the time elapsed during unloading were analyzed for individual serrations. Figure 2 is a plot of load versus time during serrated flow in $Zr_{40}Ti_{14}Ni_{10}Cu_{12}Be_{24}$, from which the magnitude of the load drop of each serration is determined. Figure 3 is a plot of the total displacement versus time for the serrations in Fig. 2, from which the total displacement during the unloading of each serration is determined. Using these data and the stiffness of the material, the elastic and plastic components of the displacement during unloading were determined. The time elapsed during the load drop of each serration is also determined from Fig. 3; however, we note that greater temporal resolution is required to definitively measure this quantity. Results with an additional data point during each unloading segment have been reported elsewhere for a different alloy.[15] Our present investigations indicate that the time elapsed during the unloading segment is approximately 5 ms.

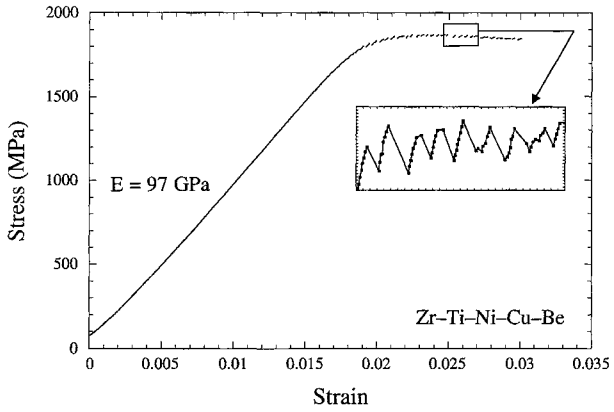

Fig. 1 Stress-strain curve for $Zr_{40}Ti_{14}Ni_{10}Cu_{12}Be_{24}$ in uniaxial compression.

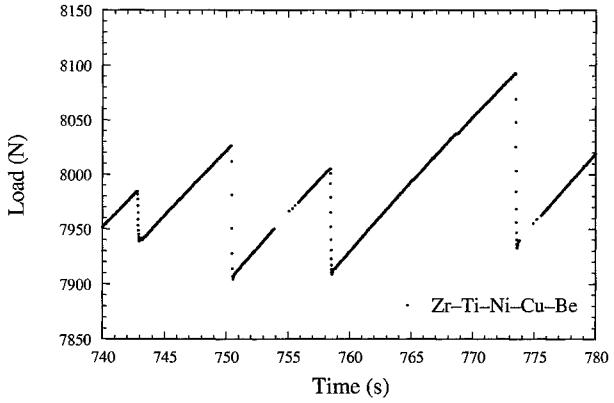

Fig. 2 Load as a function of time in serrated flow region of $Zr_{40}Ti_{14}Ni_{10}Cu_{12}Be_{24}$ tested in uniaxial compression.

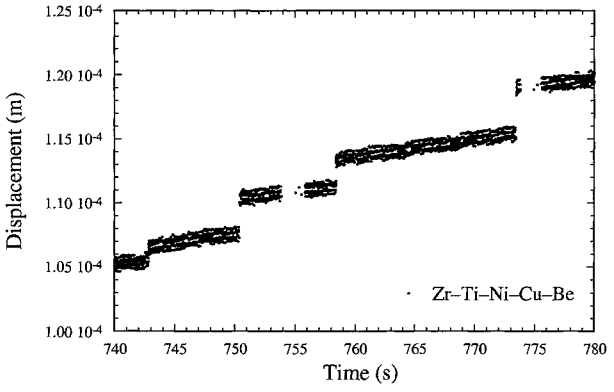

Fig. 3 Total displacement as a function of time in serrated flow region of $Zr_{40}Ti_{14}Ni_{10}Cu_{12}Be_{24}$ tested in uniaxial compression. Data is for the same serrations as shown in Figure 2.

Figure 4 is a scanning electron micrograph of the surface of the offset of a shear band formed during quasi-static compression of $Zr_{40}Ti_{14}Ni_{10}Cu_{12}Be_{24}$. There is no evidence of melting on this surface. Figure 5 is a scanning electron micro-

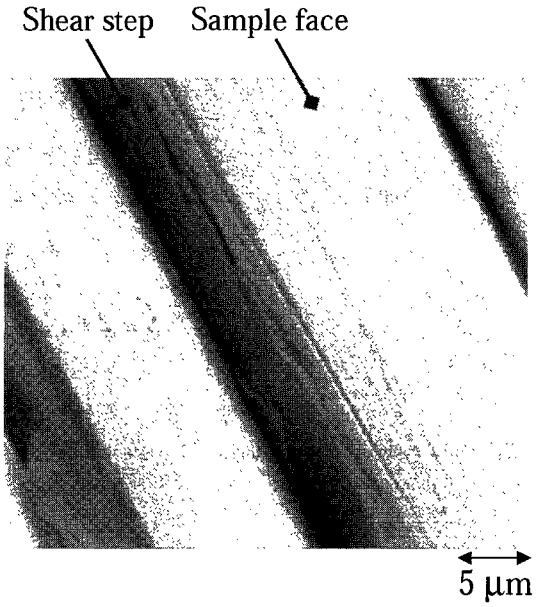

Fig. 4 Scanning electron micrograph of the surface of the offset of a shear band formed during quasi-static uniaxial compression of $Zr_{40}Ti_{14}Ni_{10}Cu_{12}Be_{24}$. There is no evidence of melting on this surface.

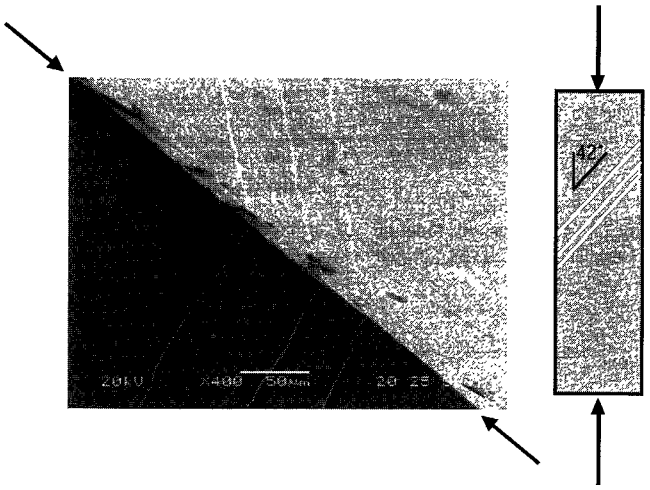

Fig. 5 Scanning electron micrograph of three shear bands formed during uniaxial compression of $Zr_{40}Ti_{14}Ni_{10}Cu_{12}Be_{24}$. The arrows indicate the loading axis. In the foreground, the shear bands are perpendicular to the edge of the sample; on the adjacent side, the shear bands form an angle of 42° with the loading axis.

graph of three shear bands, also formed during compression. The arrows indicate the loading axis. In the foreground, the shear bands are perpendicular to the edge of the sample; on the adjacent side, the shear bands form an angle of 42° with the loading axis. Because the shear bands are perpendicular to the edge of the sample on one side, the orientation of the bands is unambiguous.

2.3 Discussion and analysis

In an earlier analysis, we considered possible local adiabatic heating in a single shear band due to the work done on the sample during plastic deformation.[15] It was assumed that the formation of each shear band is manifested in a single serration and that all of the work done in producing the shear band is dissipated as heat. It was also assumed that shear occurred simultaneously over the entire band. Using the data described above, these assumptions led to an estimate of the local temperature rise on the plane of the shear band according to an expression derived by Carslaw and Jaeger[16] and applied to shear band heating by Eshelby and Pratt.[17] The predicted temperature increases were on the order of a few degrees Kelvin. It is likely, however, that rather than occurring simultaneously over the entire shear band, shear initiates at one point in the band and then propagates. If this is indeed the case, the previous model would overestimate the area being heated, thereby underestimating the temperature increase. For this reason, we now consider a second model in which heating occurs over a more localized area as shear propagates progressively across the sample.

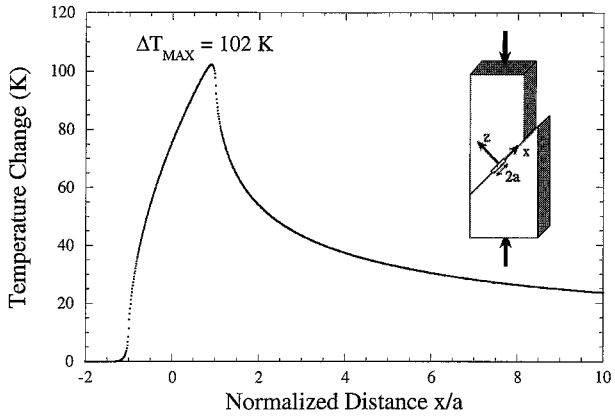

Fig. 6 Temperature change in the plane of a shear band in $Zr_{40}Ti_{14}Ni_{10}Cu_{12}Be_{24}$ as a function of distance from the heat source based on measurements of serrated plastic flow and eq. (3).

In this model, we again assume that the formation of each shear band is manifested in a single serration and that all of the work done in producing the shear band is dissipated as heat. We consider the boundary between the sheared and unsheared material to be a macroscopic defect and treat the core of this defect as a process zone in which heat is generated. The heat source is modeled as a planar slit with width $2a$ as illustrated in Fig. 6. Heat is generated at the rate $\dot{Q}$ per unit time per unit length over the slit. $\dot{Q}$ is given by $\dot{Q} = \tau u_{\text{plastic}} V$, where τ is the applied shear stress, u_{plastic} is the plastic displacement in the plane of the shear band, and V is the velocity of the heat source as it propagates across the sample. The shear bands occur in uniaxial compression at an angle φ with respect to the loading axis such that $u_{\text{plastic}} = \Delta d_{\text{plastic}}/\cos\varphi$, where $\Delta d_{\text{plastic}}$ is the plastic displacement that occurs in the direction of the loading axis during the unloading of a single serration. The total displacement during unloading Δd_{total} is the sum of elastic and plastic components, such that the plastic component is given by

$$\Delta d_{\text{plastic}} = \Delta d_{\text{total}} - \frac{\Delta P}{k}, \tag{1}$$

where ΔP is the change of load during unloading, k is the sample stiffness, and the ratio of ΔP to k is the elastic component of the displacement that occurs during the unloading of a single serration. Since ΔP is negative during unloading, the elastic component of the displacement is also negative, and the plastic displacement is larger than the total displace-

ment. The velocity of the heat source is given by $V = l/\Delta t$, where l is the length of the shear band and Δt is the time elapsed during the unloading segment of a single serration. The half-width of the slit, a, is a measure of the width of the process zone. We estimate a according to the equation for the radius of the core of a screw dislocation, $a = b/(2\pi\gamma)$, where b is the effective Burgers vector of the macroscopic dislocation under consideration and γ is the elastic strain that may be supported by the glass. The elastic strain γ is given by $\gamma = \tau_{\text{yield}}/G$, where τ_{yield} is the shear yield strength of the material and G is the shear modulus. We estimate the length of the Burgers vector as the plastic displacement that occurs during the unloading segment of a single serration and find the size of the process zone to be

$$a = \frac{u_{\text{plastic}} G}{2\pi \tau_{\text{yield}}}. \tag{2}$$

The plastic displacement as determined from the serrated flow data is consistent with the length of the step formed by a shear band at the edge of a sample as observed with scanning electron microscopy.

Using the parameters defined above, the temperature change at a point for a planar heat source moving in the direction of the negative x-axis, as derived by Carslaw and Jaeger,[16] is given by

$$\Delta T(x, z) = \frac{\dot{Q}}{4\pi K}\frac{1}{a}\int_{-a}^{a} \exp\left[\frac{V(x-x')}{2\kappa}\right] \times K_0\left(\frac{V\sqrt{(x-x')^2+z^2}}{2\kappa}\right) dx', \tag{3}$$

where z is the position coordinate along the direction perpendicular to the plane of the shear band, K is the thermal conductivity, κ is the thermal diffusivity, and K_0 is the modified Bessel function of the second kind of order zero. The prediction of this model for the temperature profile in the plane of a shear band, based on the data for a single serration and the thermal constants for this alloy, is shown in Fig. 6. The predicted maximum temperature increase generated by the heat source as each shear band propagates in $Zr_{40}Ti_{14}Ni_{10}Cu_{12}Be_{24}$ ranges from 90 to 120 K, and the predicted maximum temperature increase for the data shown in Fig. 6 is 102 K. The heat source is moving in the negative x-direction, and there is a negligible temperature change in front of the heat source because that material has not yet sheared. The temperature profile is sharply peaked within the process zone region. There is a residual temperature increase behind the heat source because the material there has just sheared, and the heat has not yet fully dissipated.

Evidence of melting on the fracture surfaces of metallic glass samples is often observed. Since the magnitude of the load drop during failure is much larger than the magnitude of the load drops that occur during serrated flow, a larger temperature increase is expected for the failure event.[15] There is, however, no evidence of melting on the surfaces of the steps formed by the shear bands at the edges of the samples as shown in Fig. 4; this is consistent with the prediction of the model.

The maximum temperature increase predicted by this model is insufficient to reach the glass transition temperature of 625 K;[1] thus, it is not a likely source of serrated flow. We note that the finite thickness of shear bands has not been used in this model; if it were, the predicted temperature increase would be even smaller. This thermal analysis, however, is sensitive to the time elapsed during the unloading segment of a single serration. If shear bands propagate faster than these experiments indicate, the temperature rise in a shear band might be large enough to significantly reduce the viscosity and possibly lead to flow localization.

In an amorphous material, it is expected that shear bands will form on planes of maximum resolved shear stress; these planes are oriented at an angle of 45° to the loading axis in uniaxial compression. As Fig. 5 reveals, shear bands formed during uniaxial compression of $Zr_{40}Ti_{14}Ni_{10}Cu_{12}Be_{24}$ are oriented at an angle of 42° to the loading axis. In uniaxial tension experiments of other Zr-based bulk metallic glasses, shear bands formed at an angle of 56° to the loading axis.[12] These deviations from the plane of maximum resolved shear suggest that the normal stress which acts across the shear plane influences shear band propagation. Donovan made a similar observation for shear band orientation in $Pd_{40}Ni_{40}P_{20}$.[3,4] Consequently, she proposed that metallic glasses follow the Mohr-Coulomb yield criterion. The Mohr-Coulomb criterion is based on an empirical approach that accounts for an increased shear resistance caused by compressive normal stresses; conversely, it predicts a decreased shear resistance for tensile normal stresses. Such a law might be applicable to amorphous materials because normal displacements are expected to occur as atoms are forced to slide past each other. The Mohr-Coulomb criterion can be expressed as

$$\tau_{\text{critical}} = k_0 - \alpha\sigma_{\text{normal}}, \tag{4}$$

where τ_{critical} is the critical resolved shear stress at which yielding occurs, k_0 is the yield strength of the material when subjected to pure shear, α is the normal stress coefficient, and σ_{normal} is the component of the applied stress which acts normal to the shear plane. An analytical expression for α is determined by expressing τ_{critical} and σ_{normal} in terms of the applied stress and the angle of inclination of the shear plane and then solving eq. (4) for the value of α at which the applied stress is a minimum. A numerical value for α is found by using the angle defining the orientation of the shear plane as determined by experiment. For $Zr_{40}Ti_{14}Ni_{10}Cu_{12}Be_{24}$, $\alpha = 0.105$.

3. Nanoindentation

We now consider the plastic flow properties of $Zr_{40}Ti_{14}Ni_{10}Cu_{12}Be_{24}$ as determined by nanoindentation. This testing technique permits the study of plasticity at microstructural length scales in crystalline materials. Our objective in this work was to determine if mechanical testing on the scale of shear bands or, perhaps, on the scale of distributed free volume would reveal useful information about the mechanism of plasticity in this glass.

3.1 Experimental procedures

The mechanical properties of $Zr_{40}Ti_{14}Ni_{10}Cu_{12}Be_{24}$ were characterized using a Nano II™ (MTS Nano Innovation Center, Oak Ridge, TN) operated in the continuous stiffness mode. The system has load and displacement resolutions

of 0.25 μN and 0.16 nm, respectively. Diamond Berkovich and conical indenters were used to perform three different experiments. The Berkovich indenter is a three-sided pyramid with the same area-to-depth function as a Vickers indenter. A Berkovich indenter was used to make large indentations to measure the elastic modulus and the hardness of $Zr_{40}Ti_{14}Ni_{10}Cu_{12}Be_{24}$; this same indenter, with a tip radius of 234 nm, was used to study the onset of plasticity at very small indentation depths. The conical indenter had a blunt tip with a large radius of curvature of 27 μm; this indenter was used to impose purely elastic deformation upon initial indentation prior to the onset of plasticity. The indentations were made at a constant nominal strain rate under load control. The samples tested in these experiments were mechanically polished with a dispersion of 0.05 μm alumina particles; similar results were obtained for samples that were electropolished to remove mechanical damage caused by polishing.

3.2 Experimental results

A series of ten indentations were made to a maximum load of 135 mN using a Berkovich indenter. Figure 7 is a plot of the load-displacement response of one of these indentations. During loading, elastic and plastic deformation occurred. The indentation depth at maximum load was 1025 nm. On unloading, the elastic deformation was recovered, and the final depth of the residual hardness impression was 750 nm.

Figure 8 is a profile of a cross-section of an indentation of $Zr_{40}Ti_{14}Ni_{10}Cu_{12}Be_{24}$ that was determined using atomic force microscopy (AFM). Pile-up is clearly observed along the sides of the triangular indentation. Because the material being deformed is amorphous, it is unable to strain harden; thus it is easier for the surrounding material to flow up around the indenter (pile-up) than to displace the material which lies further below the indentation.[18]

Figure 9 is a plot of the elastic modulus of $Zr_{40}Ti_{14}Ni_{10}Cu_{12}Be_{24}$ as a function of indentation depth. The elastic modulus was calculated using the method of Oliver and Pharr,[19] and the results shown are an average of ten indentations. The elastic modulus of fused silica as a function of indentation depth is also shown; fused silica serves as a reference material and validates the accuracy of the tip shape calibration because its elastic modulus has the expected value of 73 GPa. The modulus of $Zr_{40}Ti_{14}Ni_{10}Cu_{12}Be_{24}$ is observed to increase from 106 GPa at small indentation depths to a constant value of 114 GPa for indentation depths greater than 200 nm. The elastic modulus calculated from the stress-strain curve in Fig. 1 is 97 GPa. The discrepancy between the elastic modulus determined from indentation experiments and from uniaxial compression testing is due to limitations in the Oliver-Pharr method, which does not account for the additional area in contact with the indenter when pile-up occurs. As a result, the contact area is underestimated, and the elastic modulus is overestimated.

Figure 10 is a plot of the true hardness of $Zr_{40}Ti_{14}Ni_{10}Cu_{12}Be_{24}$ as a function of indentation depth; the results shown

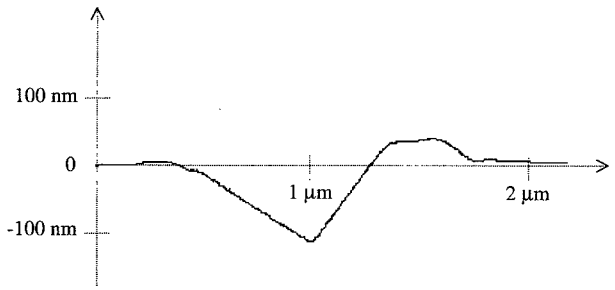

Fig. 8 An AFM profile of a cross-section of an indentation showing the material pile-up along the sides of the triangular indentation.

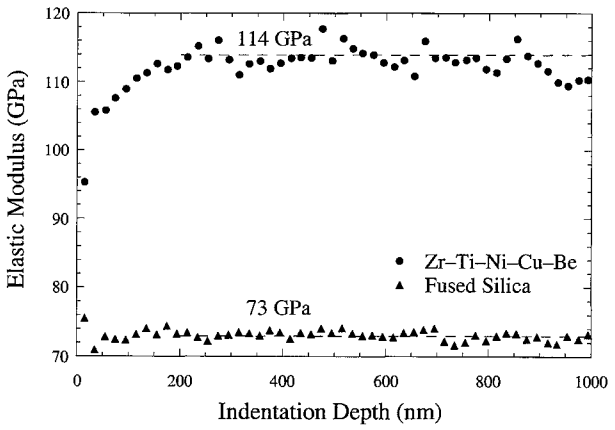

Fig. 9 Elastic modulus as a function of indentation depth for $Zr_{40}Ti_{14}Ni_{10}Cu_{12}Be_{24}$ and fused silica.

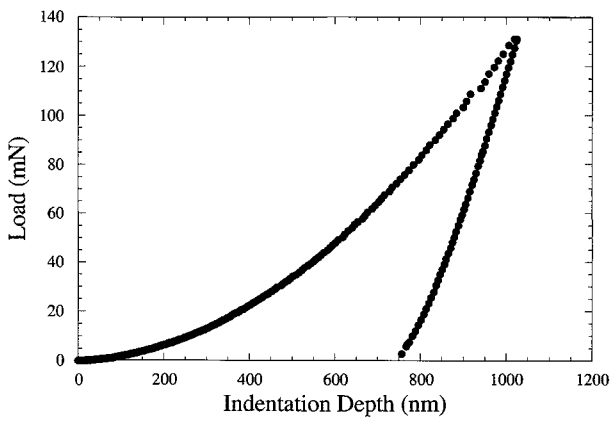

Fig. 7 Load as a function of displacement for an indentation of $Zr_{40}Ti_{14}Ni_{10}Cu_{12}Be_{24}$ using a Berkovich indenter.

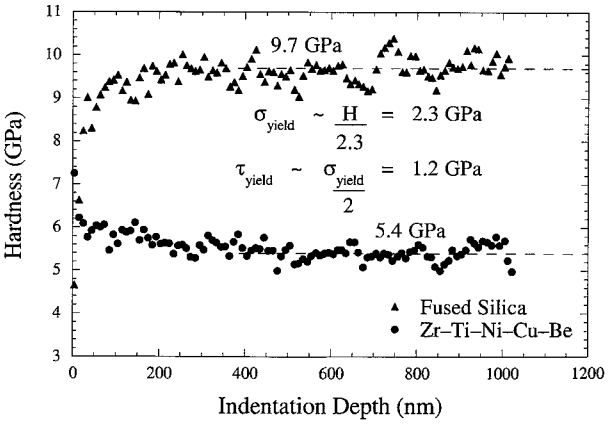

Fig. 10 True hardness as a function of indentation depth for $Zr_{40}Ti_{14}Ni_{10}Cu_{12}Be_{24}$ and fused silica.

are based on contact areas determined from the measured stiffness[20] and thus account for the effect of pile-up. The hardness of $Zr_{40}Ti_{14}Ni_{10}Cu_{12}Be_{24}$ is 5.4 GPa at depths greater than 200 nm. Again the hardness of fused silica has been plotted for comparison, and it has the expected hardness of 9.7 GPa.

We now consider the initial stage of indentation, when the diamond tip first makes contact with the surface of the glass. For purely elastic contacts, the indenting load P can be related to the indenter displacement h using the Hertz theory of normal contact between two frictionless elastic solids:

$$P = \frac{4}{3}E_r\sqrt{R}h^{3/2}, \tag{5}$$

where R is the radius of curvature of the indenter tip and E_r is the reduced modulus.[21] The reduced modulus accounts for the effects of a non-rigid indenter on the load-displacement behavior and is computed as

$$\frac{1}{E_r} = \frac{1-\nu^2}{E} + \frac{1-\nu_i^2}{E_i}, \tag{6}$$

where E and ν are the elastic modulus and Poisson's ratio of the material being indented and E_i and ν_i are the elastic modulus and Poisson's ratio of the indenter. In crystalline materials, the elastic-plastic transition can be observed in the indentation load-displacement data if the material is initially dislocation-free. Figure 11 is a plot of the indentation load-displacement response of a single crystal Mo film deposited epitaxially on a MgO substrate. The elastic nature of the contact for indentation depths of less than 8 nm is confirmed by agreement between the experimental data and a plot of eq. (5) using the calibrated tip radius and the elastic constants of Mo. Several sudden, discrete increases in displacement, called "pop-ins," are observed at indentation depths greater than 8 nm; these are attributed to dislocation nucleation events. Figure 12 is a plot of the indentation load-displacement response for $Zr_{40}Ti_{14}Ni_{10}Cu_{12}Be_{24}$ when indented by a conical tip with a radius of curvature of 27 μm. The contact between the indenter and material is purely elastic for depths less than 252 nm, and the elastic modulus is computed to be 97 GPa using the Hertz theory. At approximately 252 nm, a sudden, discrete jump in displacement, similar to the pop-ins observed in crystalline materials, occurs. Such an event in an amorphous material cannot be attributed to a dislocation nucleation event, but it may be related to shear band formation. At depths greater than 252 nm, $Zr_{40}Ti_{14}Ni_{10}Cu_{12}Be_{24}$ deforms plastically as evidenced by the deviation of the load-displacement data from Hertz-like behavior. Thus the pop-in marks the onset of plasticity.

Figure 13 is a plot of the load-displacement response of $Zr_{40}Ti_{14}Ni_{10}Cu_{12}Be_{24}$ at shallow indentation depths when indented by the Berkovich tip with a radius of curvature of 234 nm. From the outset, $Zr_{40}Ti_{14}Ni_{10}Cu_{12}Be_{24}$ deforms both elastically and inelastically as indicated by the fact that the apparent elastic modulus computed using the Hertz theory is only 80 GPa, less than the expected 97 GPa. We assume that atomic rearrangements at the surface may be responsible for this inelasticity. The modulus here is smaller than the modulus determined using the conical tip because the Hertz theory does not account for the additional displacements of inelastic deformation. A pop-in is observed at an indentation depth of 11.5 nm. Again plasticity is observed as the deviation of the data from Hertz-like behavior.

3.3 Discussion and analysis

The yield strength of a material under uniaxial compres-

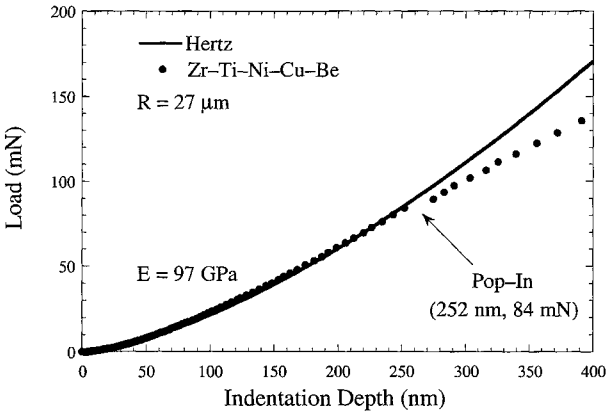

Fig. 12 Load as a function of displacement for an indentation of $Zr_{40}Ti_{14}Ni_{10}Cu_{12}Be_{24}$ with a conical tip with a radius of curvature of 27 μm. A pop-in is observed at a load of 84 mN and a depth of 252 nm.

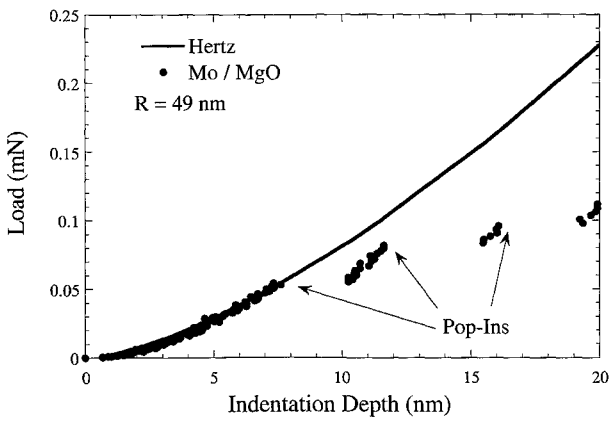

Fig. 11 Load as a function of displacement for an indentation of a single crystal Mo film deposited epitaxially on a MgO substrate. Pop-ins are observed at indentation depths greater than 8 nm.

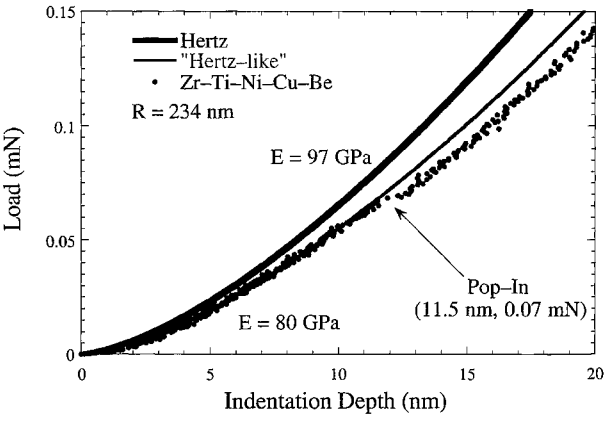

Fig. 13 Load as a function of displacement for $Zr_{40}Ti_{14}Ni_{10}Cu_{12}Be_{24}$ at shallow indentation depths when indented by a Berkovich tip with a radius of curvature of 234 nm. A pop-in is observed at a load of 0.07 mN and a depth of 11.5 nm.

sion is related to the hardness determined from indentation according to

$$\sigma_{\text{yield}} = \frac{H}{C}, \tag{7}$$

where σ_{yield} is the yield stress, H is the hardness, and C is a constant that depends on the ratio of elastic modulus to yield stress and the indenter shape.[22] For $Zr_{40}Ti_{14}Ni_{10}Cu_{12}Be_{24}$, tested with a Berkovich indenter, C is approximately equal to 2.3.[23] Using this value of C and the hardness value of 5.4 GPa from Fig. 10, the yield strength of $Zr_{40}Ti_{14}Ni_{10}Cu_{12}Be_{24}$ for an indentation to a depth of 1025 nm is calculated to be 2.3 GPa. For uniaxial compression, the shear yield strength is approximately half of the compressive yield strength such that the shear yield strength is approximately 1.2 GPa. We note that this is more than 20% higher than the shear yield strength determined by compression testing of bulk samples.

We now consider the early stage of indentation when the displacements are entirely elastic. We define a cylindrical coordinate system in which z denotes the direction parallel to the indentation axis, and r and θ denote the radial and circumferential directions, respectively. The principal stresses along the z-axis in an elastic half space due to the Hertz pressure applied to a circular region from a spherical tip are given by

$$\sigma_r = \sigma_\theta = p_0 \left\{ -(1+\nu)\left[1 - \frac{z}{a}\tan^{-1}\left(\frac{a}{z}\right)\right] + \frac{1}{2}\left(1+\frac{z^2}{a^2}\right)^{-1} \right\} \tag{8}$$

and

$$\sigma_z = -p_0 \left(1+\frac{z^2}{a^2}\right)^{-1}, \tag{9}$$

where p_0 is the maximum pressure under the indenter, ν is the Poisson's ratio of the material being indented, a is the radius of the contact circle, and z is the depth where the stresses are to be evaluated.[21] According to the Hertz theory, the maximum pressure under the indenter is given by

$$p_0 = \left(\frac{6PE_r^2}{\pi^3 R^2}\right)^{\frac{1}{3}}, \tag{10}$$

where P is the total load imposed by the indenter, R is the radius of the indenter, and E_r is given by eq. (6). The radius of the contact circle is a function of the depth of indentation and is given by

$$a = \sqrt{Rh - \left(\frac{h}{2}\right)^2}. \tag{11}$$

Thus the principal stresses along the z-axis are defined according to eqs. (8)–(11). The magnitude of the shear stress on a plane inclined by an angle β to the horizontal is then given by

$$\tau = |(\sigma_z - \sigma_r)\sin\beta\cos\beta|. \tag{12}$$

We assume that the Mohr-Coulomb analysis presented in eq. (4) is a valid yield criterion for indentation of metallic glasses. With

$$\sigma_{\text{normal}} = \sigma_r \sin^2\beta + \sigma_z \cos^2\beta, \tag{13}$$

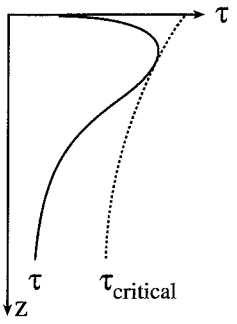

Fig. 14 Schematic diagram illustrating the application of the Mohr-Coulomb yield criterion to nanoindentation.

Equation (4) is expressed as

$$\tau_{\text{critical}} = k_0 - \alpha(\sigma_r \sin^2\beta + \sigma_z \cos^2\beta). \tag{14}$$

We assume that α is constant and equal to the value found from uniaxial compression experiments. We also assume that yielding will occur on a plane inclined by 42° to the loading axis as for uniaxial compression, such that $\beta = 48°$. We justify this assumption by considering a volume element beneath the indenter. This stress state is the sum of a state of pure uniaxial compression and a state of pure hydrostatic compression. Hydrostatic stress does not influence shear band orientation; hence, a shear band formed during nanoindentation should have the same orientation as a shear band formed during uniaxial compression.

Figure 14 is a schematic diagram for the application of the Mohr-Coulomb yield criterion to nanoindentation. The metallic glass will yield when

$$\tau = \tau_{\text{critical}}. \tag{15}$$

The slopes of the curves for τ and τ_{critical} must also be equal at the indentation depth where yielding first occurs such that

$$\frac{\partial \tau}{\partial z} = \frac{\partial \tau_{\text{critical}}}{\partial z}. \tag{16}$$

Equations (15) and (16) thus comprise two equations with two unknown quantities: k_0, the yield strength of the material when subjected to pure shear, and z, the depth at which yielding first occurs.

Equations (15) and (16) can be solved to determine the shear yield strength of $Zr_{40}Ti_{14}Ni_{10}Cu_{12}Be_{24}$ for the indentations shown in Figs. 12 and 13. It is assumed that the first pop-in observed marks the yielding of the material; thus, P and h are determined from the data at the point where the first pop-in occurs. For indentations using the conical indenter, the shear yield strength of the material is calculated to be 1.5 GPa. For indentations using the Berkovich indenter, the shear yield strength of the material is calculated to be 2.9 GPa. As Table 1 shows, the shear yield strength of $Zr_{40}Ti_{14}Ni_{10}Cu_{12}Be_{24}$ increases as the deformed volume decreases. For uniaxial compression experiments, the shear yield strength is approximately 0.95 GPa. The shear yield strength increases to 2.9 GPa for the smallest indentations made. This size dependence for plasticity may be related to the distribution of free volume in the glass. As larger volumes of material are tested, lower shear strengths may be expected based on the probability of finding sites with larger free volume. For the indentations made with the Berkovich indenter,

Table 1 Shear yield strength as a function of deformed volume. As the deformed volume decreases, shear yield strength increases.

Indentation depth	Shear strength (GPa)
Bulk	0.95
1025 nm	1.2
252 nm	1.5
11.5 nm	2.9

the calculated values of the shear yield strength range from ±30% of the reported value. This may be the result of sampling different amounts of free volume at various locations.

4. Summary

Local adiabatic heating is not the primary cause of flow localization in metallic glasses although significant heating is predicted for the final failure event. The free volume theory of deformation is consistent with both the orientation of shear bands in compression samples and an indentation size effect for the onset of plastic flow in nanoindentation.

Acknowledgements

The assistance of Professor D. M. Barnett (heat modeling) and R. E. Jones (microscopy) is greatly appreciated. This work was supported by the Air Force Office of Scientific Research under AFOSR Grant No. F49620-98-1-0260. A Stanford Graduate Fellowship and a National Science Foundation Graduate Research Fellowship supported W. J. Wright.

REFERENCES

1) A. Peker and W. L. Johnson: Appl. Phys. Lett. **63** (1993) 2342.
2) A. Inoue: Mater. Trans., JIM **36** (1995) 866.
3) P. E. Donovan: Mater. Sci. Eng. **98** (1988) 487.
4) P. E. Donovan: Acta Metall. **37** (1989) 445.
5) H. A. Bruck, T. Christman, A. J. Rosakis and W. L. Johnson: Scripta Metall. Mater. **30** (1994) 429.
6) R. D. Conner, A. J. Rosakis, W. L. Johnson and D. M. Owen: Scripta Mater. **37** (1997) 1373.
7) C. J. Gilbert, R. O. Ritchie and W. L. Johnson: Appl. Phys. Lett. **71** (1997) 476.
8) F. Spaepen: Acta Metall. **25** (1977) 407.
9) A. S. Argon: Acta Metall. **27** (1979) 47.
10) P. S. Steif, F. Spaepen and J. W. Hutchinson: Acta Metall. **30** (1982) 447.
11) H. J. Leamy, H. S. Chen and T. T. Wang: Metall. Trans. **3** (1972) 699.
12) C. T. Liu, L. Heatherly, D. S. Easton, C. A. Carmichael, J. H. Schneibel, C. H. Chen, J. L. Wright, M. H. Yoo, J. A. Horton and A. Inoue: Metall. Mater. Trans. **29A** (1998) 1811.
13) H. A. Bruck, A. J. Rosakis and W. L. Johnson: J. Mater. Res. **11** (1996) 503.
14) H. S. Chen: Scr. Metall. **7** (1973) 931.
15) W. J. Wright, R. B. Schwarz and W. D. Nix: to appear in Mater. Sci. Eng. A.
16) H. S. Carslaw and J. C. Jaeger: *Conduction of Heat in Solids*, (Oxford University Press, London, 1959) p. 75, p. 269.
17) J. D. Eshelby and P. L. Pratt: Acta Metall. **4** (1956) 560.
18) K. W. McElhaney, J. J. Vlassak and W. D. Nix: J. Mater. Res. **5** (1998) 1300.
19) W. C. Oliver and G. M. Pharr: J. Mater. Res. **7** (1992) 1564.
20) D. L. Joslin and W. C. Oliver: J. Mater. Res. **5** (1990) 123.
21) K. L. Johnson: *Contact Mechanics*, (Cambridge University Press, Cambridge, 1985) p. 93, p. 62.
22) K. L. Johnson: J. Mech. Phys. Solids **18** (1970) 115.
23) A. K. Bhattacharya and W. D. Nix: Int. J. Solids Structures **24** (1988) 881.